ASTRONOMY

The Moon's farside shallow subsurface structure unveiled by Chang'E-4 Lunar Penetrating Radar

Chunlai Li[1,2], Yan Su[1,2]*, Elena Pettinelli[3]*, Shuguo Xing[1]*, Chunyu Ding[4], Jianjun Liu[1,2], Xin Ren[1], Sebastian E. Lauro[3], Francesco Soldovieri[5], Xingguo Zeng[1], Xingye Gao[1], Wangli Chen[1], Shun Dai[1], Dawei Liu[1], Guangliang Zhang[1], Wei Zuo[1,2], Weibin Wen[1], Zhoubin Zhang[1], Xiaoxia Zhang[1], Hongbo Zhang[1]

On 3 January 2019, China's Chang'E-4 (CE-4) successfully landed on the eastern floor of Von Kármán crater within the South Pole–Aitken Basin, becoming the first spacecraft in history to land on the Moon's farside. Here, we report the observations made by the Lunar Penetrating Radar (LPR) onboard the Yutu-2 rover during the first two lunar days. We found a signal penetration at the CE-4 landing site that is much greater than that at the CE-3 site. The CE-4 LPR images provide clear information about the structure of the subsurface, which is primarily made of low-loss, highly porous, granular materials with embedded boulders of different sizes; the images also indicate that the top of the mare basal layer should be deeper than 40 m. These results represent the first high-resolution image of a lunar ejecta sequence ever produced and the first direct measurement of its thickness and internal architecture.

INTRODUCTION

The stratigraphic architecture of the lunar subsurface is the result of a complex and long process of emplacement and modification of the deposited materials (*1*). Such architecture can be inferred from remote sensing observations (*2*) or can be directly imaged using geophysical techniques like seismic or electromagnetic wave prospections (*3*). Both methods were successfully tested during the Apollo missions, providing ground-breaking information about the Lunar interior. In the past 20 years, spaceborne/rover-deployed Ground Penetrating Radar (GPR) has progressively become the most suitable geophysical technique to investigate planetary subsurface stratigraphy. Two orbiting radars were hosted on NASA's Apollo 17 and Japan Aerospace Exploration Agency's Kaguya missions, the Apollo Lunar Sounder Experiment and Kaguya Lunar Radar Sounder (*4*, *5*), which were able to survey the subsurface structure down to a depth of 1 to 2 km. The first attempt to survey the Moon's subsurface using a GPR onboard a rover was made during the Chang'E-3 (CE-3) mission, which was equipped with low- and high-frequency antennas (*6*). The high-frequency GPR observations revealed a detailed subsurface structure up to a depth of about 10 m (*7*). Conversely, interpretation of the low-frequency data remains quite controversial due to antenna coupling with the rover and the lunar surface, combined with the limited length of the radar profile (*8*–*10*).

On 3 January 2019, the Chang'E-4 (CE-4) lander touched down on the eastern floor of Von Kármán crater at 45.4446°S, 177.5991°E (Fig. 1A) (*11*, *12*), becoming the first spacecraft to land safely on the Moon's farside. The Yutu-2 rover, equipped with the same dual-frequency Lunar Penetrating Radar (LPR) as CE-3, was successfully deployed to the surface about 12 hours later. The pre-Nectarian Von Kármán crater (44.45°S, 176.3°E; diameter equal to about 186.3 km) is located in the northwestern sector of the South Pole–Aitken basin, the oldest and largest impact structure on the Moon (*13*). The overall terrain of Von Kármán crater is relatively flat, and its floor was flooded by Imbrian-aged mare basalts that appear dark in optical images (*14*). The absolute model age of the mare basalts was dated to be ~3.6 billion years (Ga) based on the size-frequency distribution of superposed impact craters (*2*, *14*). Judging from the remote optical and multispectral images, a large portion of mare basalt was later overprinted by distal ejecta that appear bright, which were most probably delivered from surrounding large craters such as Finsen and Von Kármán L (*2*). As a result, secondary craters are widespread over the floor of Von Kármán, as indicated by their spatial patterns (e.g., chains or clusters with herringbone-shaped morphology) (*2*, *15*). The CE-4 spacecraft landed on the bright distal ejecta from surrounding large craters (Fig. 1A and fig. S8), in an area with a low abundance of rocks and boulders on the surface (fig. S1).

The CE-4 LPR is a dual-frequency GPR system, operating at 60 MHz (low frequency) and 500 MHz (high frequency), with a frequency band of 40 to 80 MHz and 250 to 750 MHz, respectively (*16*, *17*). The radar data were collected during the first two lunar days along the Yutu-2 route (Fig. 1B). In this work, we processed and interpreted only the high-frequency LPR data. As in the CE-3 mission, the low-frequency antennas are installed on the back of the CE-4 rover; unfortunately, this leads to electromagnetic coupling with the rover's metallic body (*18*), resulting in strong disturbances that largely overlap the signals coming from the subsurface. These disturbances could easily be misinterpreted as subsurface reflectors (*10*), and thus, more data should be acquired to effectively mitigate/remove these artifacts from the radargram.

RESULTS

LPR image and physical parameter estimation

The collected high-frequency radar data from point A to point LE210 (Fig. 1B) were processed using standard GPR signal processing methods (fig. S2) [e.g., (*19*)] and are represented as a seismic color image (radargram) (Fig. 2A). The radar section indicates a very good signal penetration, and radar features are well detectable down

[1]Key Laboratory of Lunar and Deep Space Exploration, National Astronomical Observatories, Chinese Academy of Sciences, Beijing 100101, China. [2]University of Chinese Academy of Sciences, Beijing 100049, China. [3]Mathematics and Physics Department of Roma Tre University, Roma 00146, Italy. [4]School of Atmospheric Sciences, Sun Yat-sen University, Zhuhai 519000, China. [5]Istituto per il Rilevamento Elettromagnetico dell'Ambiente IREA-CNR, I-80124 Naples, Italy.
*Corresponding author. Email: suyan@nao.cas.cn (Y.S.); pettinelli@fis.uniroma3.it (E.P.); xingsg@nao.cas.cn (S.X.)

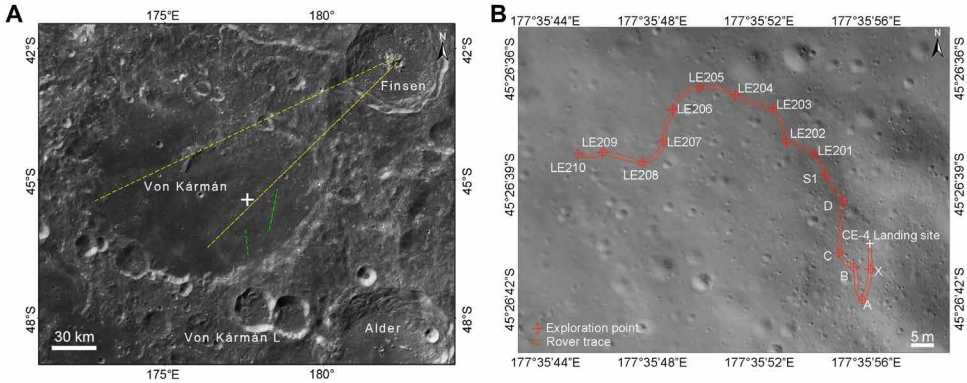

Fig. 1. The CE-4 landing region and the Yutu-2 rover route. (**A**) CE-4 landed in the eastern floor of Von Kármán crater (44.45°S, 176.3°E; diameter ~186.3 km), as indicated by the white cross (177.5991°E, 45.4446°S) on a bright ejecta blanket. The yellow and green lines show the ejecta direction from Finsen (*12*) and Von Kármán L, respectively. The image is CE-2 7-m resolution Digital Orthophoto Map (DOM). (**B**) Yutu-2 rover route during the first two lunar days. Two red lines show the tracks of the left and right wheels on the Yutu-2 rover. The LPR performed observation along the ~106-m route from exploration points A to LE210. The background image is mosaicked from images obtained during the landing process, where the spatial resolution is 5 cm.

to a two-way travel time of about 500 ns. This penetration is much larger (over three times in terms of two-way travel time) than that reached by the CE-3 LPR at the Zi Wei crater landing site (for comparison, see fig. S3). As a result, the subsurface at the CE-4 landing site is much more transparent to radio waves, and this qualitative observation suggests a totally different geological context for the two landing sites. A quantitative estimation of the signal attenuation in the subsurface material is given by the loss tangent value (*20*), which, for the CE-4 landing site, was estimated to be $\tan\delta = (5 \pm 2) \times 10^{-3}$; this value appears to preclude an intact, dense lava flow layer in this sequence, because such a material would increase the loss tangent ($\tan\delta > 10^{-2}$) and prevent deep penetration (*21*).

The stratigraphic sequence illustrated in the radargram (Fig. 2A) does not show any sharp and continuous reflectors that extend across the entire radar profile, but rather, it appears to be made of a complex distribution of radar features that cluster in specific areas. Two main depth sections can be identified: an initial section (about 0 to 150 ns) that, aside from a few scattered hyperbolic reflectors (fig. S4), appears fairly uniform and very transparent to radio waves, and a second section (about 150 to 500 ns) that is much more irregular, with areas of strong discontinuous reflectors alternating with more uniform and transparent intervals (Fig. 2A). Below ~500 ns, no evident radar features are detectable. To convert the two-way travel time into depth, an estimation of the electromagnetic wave velocity is necessary, which we calculated by applying the hyperbola calibration method. Using seven well-defined point-source hyperbolic events, which are only present within the first section (between 30 and 90 ns), we computed the average wave velocity at different time delays (fig. S4). Such velocity progressively decreases and reaches a constant value, $v = 0.16$ m/ns, at about 70 ns. Given the lack of any other information, we assumed that this velocity does not appreciably change with depth and that it does not vary across the entire radar section. On the basis of this value, the thickness of the homogeneous material at the top of the radar section (0 to 150 ns) is about 12 m, whereas the underlying material (150 to 500 ns) is about 28 m thick. We used the set of retrieved velocity values to estimate the material bulk density in the first 7 m (fig. S5) of the radar section. Applying two different models (*22*, *23*), we obtained two slightly different trends reaching the asymptotic values 1.90 ± 0.08 g/cm^3 (*22*) and 1.67 ± 0.07 g/cm^3 (*23*) at about 5.8 m depth. Last, applying the relationship between loss tangent, density, and oxide content defined for the lunar nearside (*21*), we compute the ($FeO + TiO_2$) abundance at the CE-4 landing site (fig. S6). We found a ($FeO + TiO_2$) content of $9 \pm 4\%$ (*22*) and $11 \pm 4\%$ (*23*), in good agreement with the range, 11.4 to 15.9%, measured by Kaguya Multiband Imager (MI) (*24*) at this site. This compatibility is quite notable, as the two techniques probe different portions of the lunar regolith: Kaguya data refer to the surface material, whereas LPR data refer to the large volume of material located to a depth of 6 m.

Tomographic reconstruction of the stratigraphic sequence

Despite the good quality of the radar image, the complexity of the spatial distribution and shape of the radar features makes identification of the geological structures/events that generated such features quite difficult (*25*). To overcome this problem, we applied a tomographic inversion algorithm (*26*) that is capable of gaining information about the size of the objects producing the radar features (scattering objects) when their dimension is larger than half of the signal wavelength (~0.2 m). The resulting image (Fig. 2B) illustrates the internal structure of the deposits, characterized by vertical and lateral inhomogeneities, with groups of boulders and rocks (of various sizes and located at different depths) intercalated with finer materials. On the basis of the distribution, quantity, and dimension of such inhomogeneities, the image can be separated in three main units (Fig. 2C). The shallower unit (depth interval, 0 to 12 m), unit 1, looks rather uniform, with sporadic large rocks distributed along the radar section. The underlying unit (depth interval, 12 to 24 m), unit 2, is composed of an upper part containing a large amount of randomly (almost evenly) distributed 0.2- to 1-m-wide rocks and a deeper part that is much more inhomogeneous in terms of both rock distribution and size. In the latter, three blocky regions, with boulder dimensions of, from left to right, 1 to 3, 0.3 to 1, and 1 m, alternate with zones of fine materials. In the bottom unit (24 to 40 m), unit 3, the boulder density distribution decreases considerably, and the rocky material is essentially localized on the top of this interval. Below 28 m, in the central part of the image, a lens of rather uniform and transparent material is clearly visible; this lens is probably made of very fine grained material with no large rocks. Beneath this, there

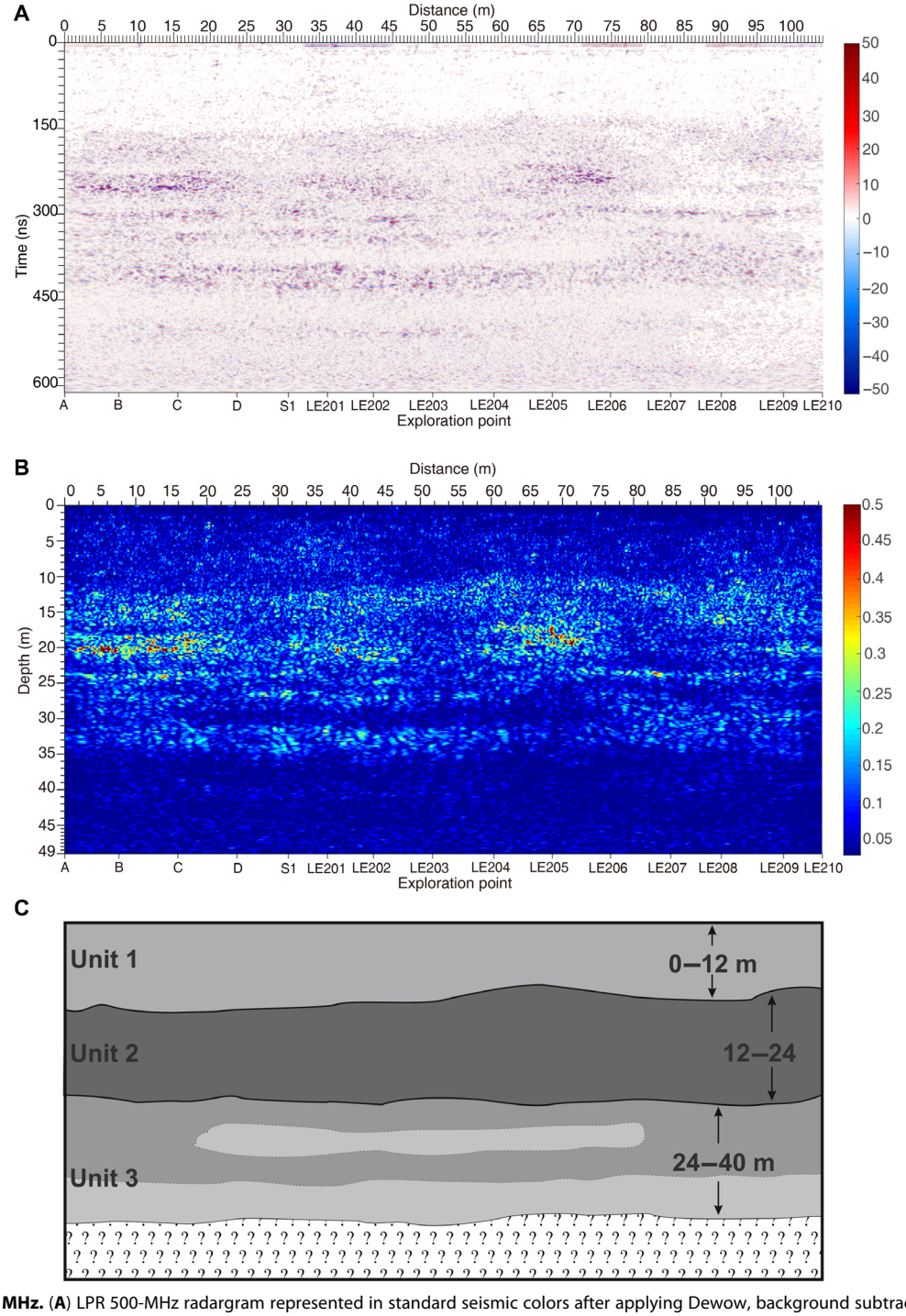

Fig. 2. LPR data at 500 MHz. (**A**) LPR 500-MHz radargram represented in standard seismic colors after applying Dewow, background subtraction, and spherical and exponential compensation (SEC) gain and migration. The *x* axis is the rover distance (top, starting point on the left) and the exploration points (bottom), and the *y* axis indicates the two-way travel time and depth; the depth is calculated on the basis of the average electromagnetic wave velocity of 0.16 m/ns. (**B**) Tomographic reconstruction of the radar data, where red represents high reflectivity (large electromagnetic contrast) and blue is low reflectivity (small electromagnetic contrast). (**C**) Schematic of the stratigraphic sequence highlighting the contacts between units and the relevant thicknesses based on the radargram (A) and the tomographic reconstruction (B). Gray tone indicates finer (light gray) or coarser (dark gray) materials.

is a zone with relative uniform distribution of small rocks overlaying a completely transparent layer and thus again probably made of very fine materials. The bottom part of this layer (40 m) is not clearly visible in the tomographic image (Fig. 2B) but is well detectable on the radargram (Fig. 2A), and it is delimited by a discontinuous distribution of poorly defined scatterers. The sequence of interposed coarser and finer materials might continue below 40 m; however, it is impossible to discriminate signal from noise at such a depth.

Ejecta thickness from DHC data

We used dark halo craters (DHCs) and non-DHCs to constrain the total thickness of distal ejecta over the landing region (*27*). Because most mare basalts in the northwest of the landing area are undisturbed and no DHCs can be found in that region, we only analyzed DHCs and non-DHCs in the area covered by ejecta in the southeast (fig. S7, A and B). Considering a radius of 20 km around the landing site, we identified 25 DHCs that have penetrated through the bright ejecta and excavated underlying dark mare basalts and 163 non-DHCs that only excavated the ejecta materials. Using the relationship between excavation depth and crater diameter (*28*), we estimated an ejecta thickness ranging from 34 to 78 m based on the DHC data (fig. S7C) and greater than 39 m based on non-DHCs located about 2 km from the landing site (fig. S7C). The observed deepest reflectors at 40 m are consistent with the lower end of this range, but the ejecta thickness may extend below this detectability limit because the ejecta thickness is estimated to be 30 to 90 m based on the excavation depth of the iron-rich craters (*29*).

DISCUSSION

Combining the information provided by the radargram, the tomographic image, and the quantitative analysis (estimated wave velocity and loss tangent), we can conclude that the subsurface internal structure at the landing site is essentially made by low-loss, highly porous granular materials embedding boulders of different sizes. Given such a strong geological constraint, the most plausible interpretation is that the sequence is made of a layer of regolith overlaying a sequence of ejecta deposits from various craters (Fig. 3), which progressively accumulated after the emplacement of the mare basalts on the floor of Von Kármán crater. The layer of regolith (unit 1) is quite thick (up to 12 m), is rather homogenous both laterally and vertically, and is mostly composed of fine materials. It developed from the uppermost portion of the ejecta deposits, which were thicker than 12 m and were delivered to this area by multiple impact craters, mostly Finsen, Von Kármán L, and Von Kármán L' craters (table S1) (*2*). Unit 2 (depth, 12 to 24 m) is characterized by large rocks and boulders that are interbedded with thin layers of fine materials. Ejecta deposition never occurs via simple carpeting, but it is accompanied by horizontal shearing and mixing, excavation, and subsurface structural disturbances (*28*), especially in areas beyond the continuous ejecta deposits of the source crater. Fine materials can be produced by the internal shearing of ejecta deposits, which reduces particle sizes, and the fine layers can also be formed due to regolith development during the intervals between different impact events. On the other hand, the CE-4 landing site is located within a secondary crater chain linked to the Finsen crater (fig. S8C), and the depth of the secondary crater is about 16 m (fig. S8D); this is the minimum depth of the structural disturbances formed during the landing of the ejecta, as the secondary crater is highly degraded. Therefore,

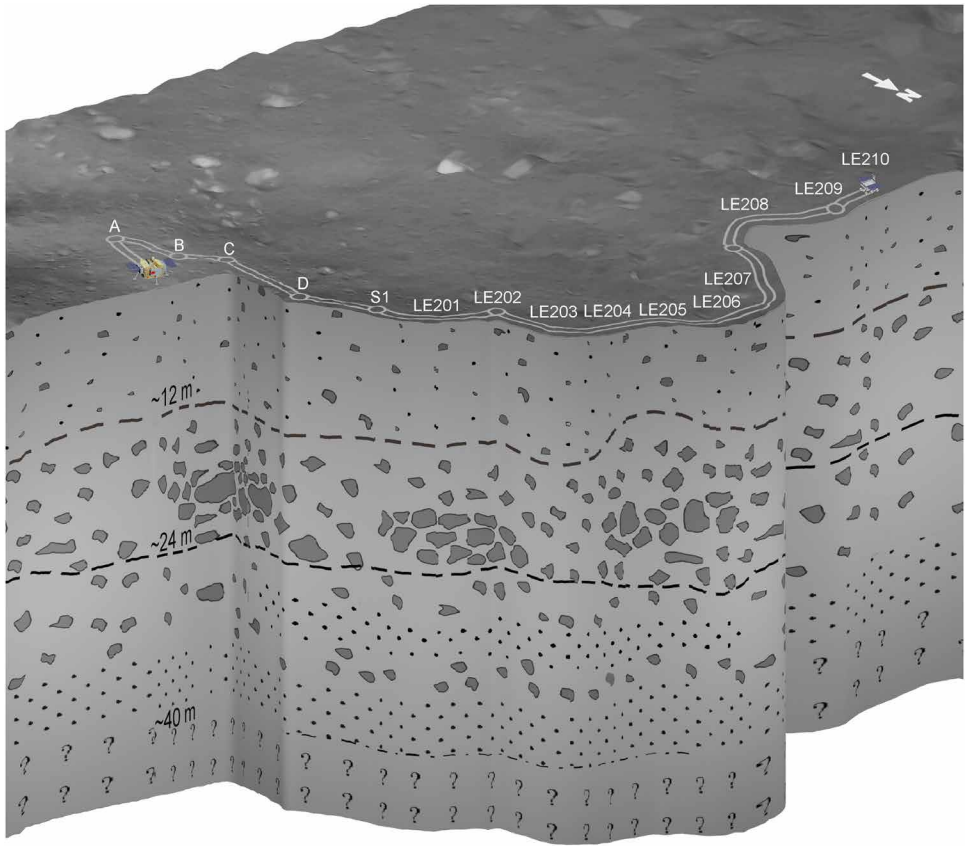

Fig. 3. Schematic representation of the subsurface geological structure at the CE-4 landing site inferred from LPR observations. The subsurface can be divided into three units: Unit 1 (up to 12 m) consists of lunar regolith, unit 2 (depth range, 12 to 24 m) consists of coarser materials with embedded rocks, and unit 3 (depth range, 24 to 40 m) contains alternating layers of coarse and fine materials.

unit 2 is likely formed due to a combination of (i) coarse ejecta that were not mobilized during the landing of impact ejecta (*28*), (ii) structural disturbances in local materials caused by the landing ejecta, and (iii) fine materials generated during or after the ejecta deposition. Unit 3 (24 to 40 m) contains alternating layers of coarse and fine materials. This unit can be interpreted as a combination of ejecta deposits, which were delivered by various craters older than Finsen and regolith developed during the impact intervals. Finsen is an Eratothenian-aged crater (<3.2 Ga), and many older craters have contributed to deliver ejecta deposits on the crater floor of Von Kármán before that age (*30*). However, tracing the source crater for each individual layer of ejecta deposits is not possible. Last, the lack of a detectable radar signal below 40 m does not allow us to make any definite conclusion about the properties of the materials at the base of the ejecta, although we can speculate that the granular materials extend beneath such a depth; accordingly, the upper contact of the mare basal layer must be deeper than 40 m.

The results of the radar data collected by the LPR during the first 2 days of lunar operation provide the first electromagnetic image of the farside subsurface structure and the first "ground truth" of the stratigraphic architecture of an ejecta deposit. The results illustrate, in an unprecedented way, the spatial distribution of the different products that contribute to form the ejecta sequence and their geometrical characteristics. The data also permitted the first unambiguous measurement of the lunar regolith layer thickness made with a radar, as previous knowledge regarding lunar soil thickness and ejecta deposition was based on impact models and indirect measurements. This work shows that the extensive use of the LPR could greatly improve our understanding of the history of lunar impact and volcanism and could shed new light on the comprehension of the geological evolution of the Moon's farside.

MATERIALS AND METHODS

LPR operation principle, data acquisition, and processing

CE-4 LPR is equipped with two distinct GPR systems. The low-frequency system is equipped with two monopole antennas having a nominal central frequency of 60 MHz and 40- to 80-MHz bandwidth. The monopoles have a length of 1.15 m and are spaced 0.8 m from each other. These antennas are installed in the back of the rover and suspended 0.6 m above the ground. The high-frequency system is equipped with one transmitting and two receiving bowtie antennas (CH2A and CH2B), with a nominal central frequency of 500 MHz and 250- to 750-MHz bandwidth. The antennas are located at the bottom of the Yutu-2 rover, ~0.3 m above the ground (contactless), and are separated 0.16 m from each other (*16*). LPR data were collected along the radar route, while the rover was traveling. The time intervals between two adjacent traces are 1.536 s at 60 MHz and 0.6636 s at 500 MHz. The velocity of the rover is ~5.5 cm/s, which gives an approximate step size of ~3.6 cm for the 500 MHz and ~8.5 cm for the 60 MHz. During the first two lunar days from point X to LE210, the LPR worked 6 hours 28 min 53 s and collected in total 13,400 and 31,749 traces at low and high frequency, respectively. In the LPR commissioning phase from point X to A, several preliminary tests were performed, and therefore, we only used LPR data collected along the route from point A to LE210 whose length is ~106 m.

Because of the strong coupling of the antennas with both the metallic rover and the lunar surface, which generates severe disturbances on the transmitted and received signals, low-frequency data have not been analyzed at this stage, as they need to be properly calibrated and accurately checked before confirming their reliability (*10*). Furthermore, because the first receiving antenna (CH2A) in the high-frequency system is affected by a strong cross-talk, we have analyzed only the data collected by the second antenna (CH2B).

The high-frequency raw data are of good quality and were processed according to the standard GPR procedure. We used a commercial software (EkkoProject V.5, Sensors and Software Inc., Canada), and we applied the following processing (*19*): (i) high-loss temporal filter, known as Dewow, to reduce the low-frequency signal due to the coupling between the receiver and the transmitter; (ii) background subtraction to suppress ring-down response; and (iii) Stolt-FK migration (*31*) using a wave velocity v = 0.16 m/ns. Moreover, we plotted the radargram using a SEC (spherical and exponential compensation) (*19*) gain in seismic standard color mode. Raw and processed data for the central part of the radar section (distance between 40 and 80 m along the profile) are shown in fig. S2. Note that the migration improves the signal to noise ratio and allows us to better detect the deeper reflectors.

Comparison between CE-3 and CE-4 data

We compared 500 MHz data collected by the LPR on board CE-3 and CE-4 (fig. S3) in terms of the maximum two-way travel time (penetration depth) at which the radar signal is still detectable. Such a comparison has been made using the same attenuation and maximum gain values applied for the radargrams shown in fig. S2C but using a different starting point for CE-3 (0.7) to better show the shallower reflectors. At the CE-4 landing site, the radar signal is detected up to a maximum two-way travel time of ~500 ns, whereas that at the CE-3 landing site is only ~150 ns. The difference in signal penetration is due to the difference in electromagnetic properties of the subsurface at the two sites, as highlighted by the loss tangent values (dictating the attenuation of the electromagnetic wave), which is $\tan\delta = (5 \pm 2) \times 10^{-3}$ for the CE-4 landing site and $\tan\delta \geq 10^{-2}$ for the CE-3 landing site (*32*) (see below).

Physical parameter estimation

Wave velocity and density

Individual targets buried in the subsurface produce different radar reflection features in the radar cross section. If the target has a size <0.1λ (where λ denotes the probing wavelength), the reflection pattern is well approximated by a hyperbola; in contrast, for objects larger than 1λ to 3λ, the reflection pattern is more complicated, while targets having a size of tens of λ generate semicontinuous, flat reflections (*33*). To convert the two-way travel time into depth, we identified seven well-defined point targets in the first interval of the section (0 to 150 ns) to estimate the radar wave velocity using the common well-established hyperbolic fitting method (fig. S4) (*19*). For each hyperbolic event, the computed value represents the average velocity in the volume of material between the surface and the point target; the estimated value decreases with depth, reaching an asymptotic limit of 0.16 m/ns at about 70 ns (5.8 m). Laboratory measurements have shown that the wave velocity (i.e., the real part of the dielectric permittivity) depends on material bulk density. Different equations relating such quantities have been proposed; here, we exploited the Olhoeft and Strangway formula (*22*)

$$\rho = 2\frac{\log(\frac{c}{v})}{\log(1.92)} \quad (1)$$

and the equation proposed by Hickson *et al.* (*23*)

$$\rho = \frac{\left(\frac{c}{v}\right)^{\frac{2}{3}} - 1}{0.307} \quad (2)$$

to compute the average density at different depths (fig. S5). In general, the density increases with depth, although the values computed using Eq. 2 (red dots in fig. S5) are systematically lower than those estimated through Eq. 1 (black dots in fig. S5), which are in good agreement with the trend (blue dashed line in fig. S5) estimated for the lunar nearside (*21*). Note that the first hyperbolic event is detectable at about 30 ns (~3 m depth), therefore far below the maximum excavation depth reached during the Apollo missions (*21*). Below 5.8 m, the density approaches a constant value, 1.90 ± 0.08 g/cm^3 according to Eq. 1 and 1.67 ± 0.07 g/cm^3 according to Eq. 2, where the uncertainties have been computed using the standard propagation formula (*34*).

Loss tangent and FeO + TiO2 abundances

The material loss factor can be computed using a frequency shift method; in the literature, there are several techniques proposed to extract such a parameter from radar data (*35*, *36*). In this work, we applied a similar approach presented in (*20*), which estimates the decrease of the centroid frequency as a function of depth in the spectrum of the LPR signal. The frequency decay has been computed for the two-way travel time from 0 to about 450 ns; thus, the average loss tangent, $\tan\delta = (5 \pm 2) \times 10^{-3}$, represents an average value for the entire radar section over that interval.

Laboratory measurements show that the loss tangent depends on bulk density and ($FeO + TiO_2$) abundance as follows (*21*)

$$\tan\delta = 10^{0.038\,(\%FeO+\%TiO_2)+0.312\rho-3.26} \quad (3)$$

Assuming a specific value for the loss tangent, we can use Eq. 3 to plot the joint probability density (*37*) as a function of bulk density and oxide content. Such distribution (fig. S6) allows us to estimate the values of the bulk density if the ($FeO + TiO_2$) content is known and vice versa. Assuming for the CE-4 landing site a loss tangent value $\tan\delta = (5 \pm 2) \times 10^{-3}$, we can use Kaguya MI (*23*) measurement (range, 11.4 to 15.9%) to estimate the bulk density (i.e., 1.4 ± 0.3 g/cm^3). On the other hand, using the bulk density values computed applying Eqs. 1 and 2, it is possible to determine the oxide content, that is, 9 ± 4% and 11 ± 4%, respectively.

Inversion tomography

The method, used to obtain the tomographic image shown in Fig. 3B, belongs to the set of migration approaches (*26*, *31*, *38*, *39*, *40*), which are based on a simplified model of electromagnetic scattering. In particular, the model underlying the migration approaches neglects the mutual interactions between the targets and allows us to estimate the properties of the buried scatterers, in terms of location and geometrical features (*26*, *39*); conversely, the quantitative reconstruction of the electromagnetic properties is possible only in the case of weak scatterers (*41*).

If we consider a point-like scatterer located in the object space at $\bar{r} = (x, y, z)$, and denote as $\bar{r}_m$, the measurement point belonging to the measurement domain Σ, and let $i(t)$ be the transmitted signal, the corresponding backscattered field is given by

$$e_s(\bar{r}_m, t) = i\left(t - 2\frac{|\bar{r}_m - \bar{r}|}{v}\right) \quad (4)$$

where the amplitude factor due to the propagation spreading has been neglected, $i(t)$ is a short-duration pulse or the pulse after range compression has occurred, and v is the velocity of the electromagnetic wave in the investigated medium. Actually, due to the finite directivity of the antennas, a point scatterer appears as a diffraction hyperboloid whose apex is located at $\left(x, y, \frac{2z}{v}\right)$, if the measurement domain Σ is located at $z = 0$. The aim of migration is to compensate such a spreading by refocusing each segment of the hyperbola to its apex. A common way to implement the migration is through the so-called diffraction summation (*38*). In this method, the object space is divided in pixels, and for each of them, a diffraction hyperboloid is built in the data space. After, the reconstruction at each pixel is achieved by summing up contributions, where the synthetic hyperboloid intersects data. From a mathematical point of view, the reconstruction is provided by $R(\bar{r})$

$$R(\bar{r}) = \int_{\Sigma}\int_{T} e_s(\bar{r}_m, t)\,\delta\left(t - 2\frac{|\bar{r}_m - \bar{r}|}{v}\right) dt\, d\bar{r}_m \quad (5)$$

where T is the time interval during which data are collected and Σ is the measurement domain over which the measurements are collected. After Fourier transforming with respect to time, Eq. 5 can be recast (apart an unessential factor) as

$$R(\bar{r}) = \int_{\Sigma}\int_{B_f} E_s(\bar{r}_m, f)\, e^{j2k|\bar{r}_m - \bar{r}|}\, df\, d\bar{r}_m \quad (6)$$

where $E_s(\bar{r}_m, f)$ is the backscattered field collected at the generic measurement point $\bar{r}_m$ and frequency f, k is the wave number in the background medium, and B_f is the working frequency band. $E_s(\bar{r}_m, f)$ is achieved by means of the Fourier transform of the GPR trace collected at the generic measurement point $\bar{r}_m$.

By sampling both the measurement domain and the working frequency band, the integral is replaced by the summation

$$R(\bar{r}) = \sum_m \sum_i E_s(\bar{r}_m, f_i)\, e^{j2k_i|\bar{r}_m - \bar{r}|}\, \Delta f \Delta \bar{r}_m \quad (7)$$

In particular, we have considered a working frequency band B_f = [250, 750] MHz sampled with a frequency step equal to Δf = 1.56 MHz (320 working frequencies). The measurement domain has an extent equal to 10 m, centered with respect to the point to be imaged and sampled with a step equal to 0.0355 m. The wave number is evaluated by assuming the relative dielectric permittivity of the subsurface equal to 3.52 (corresponding to a velocity of the electromagnetic wave equal to 0.16 m/ns).

We present the tomographic image as the modulus of the radar reflectivity map $|R(\bar{r})|$ that accounts for the location and geometry of the scattering objects inside the investigation domain. In particular, the investigation domain has a horizontal extent of 106 m and a depth ranging from 0 to 48.9 m. The dimensions of the objects were computed by evaluating the transverse extent (along x axis) of the focused spots on the tomographic image.

Ejecta thickness estimation using impact craters

We estimated the thickness of ejecta using the excavation depth of DHCs and non-DHCs. Because most mare basalts in the northwest of the landing area are undisturbed and no DHCs can be found in this region, we only analyzed DHCs and non-DHCs in ejecta blanket southeast of the landing site. In fig. S7 (A and B), we identified a total of 25 DHCs (red circles) with diameters of 327 to 1064 m and 163 non-DHCs (yellow circles) with diameters of 34 to 777 m within

a distance of 20 km from the CE-4 landing site (the white cross) in the CE-2 Digital Orthophoto Map (DOM) and the Kaguya Multiband Imager (MI) map. DHCs are thought to have penetrated the ejecta layer, so an upper limit of the ejecta thickness can be estimated, whereas non-DHCs did not penetrate the ejecta, and hence, a lower limit of the ejecta thickness can be obtained (*27*). Using the 1/10 relation between excavation depth and the transient crater diameter (which is 0.84 of the final diameter), the excavation depth (t) of an impact crater is calculated as $t = 0.084D$, where D is the final rim-to-rim diameter (*28*). Figure S7C shows the excavation depth as a function of distance from the CE-4 landing site. From this figure, excavation depths from DHCs are generally larger than those from non-DHCs, as expected. Using the 5 and 95% percentiles of DHC diameters (405 and 924 m), 90% of the surface have an ejecta thickness of 34 to 78 m. However, there are several cases where excavation depths from DHCs are less than those from non-DHCs, indicating lateral variations of ejecta thickness. Using the non-DHCs 2 km within the landing site, the distal eject thickness should be at least larger than 39 m. All these numbers are consistent with the subsurface reflectors at 40 m, indicating that ejecta should be thicker than this value.

Ejecta thickness model

We used a power function of ejecta thickness (*42*) to estimate the thickness of distal ejecta at the CE-4 landing site. The ejecta thickness t can be modeled as

$$t = T\left(\frac{r}{R}\right)^{-3} \tag{8}$$

where r is the distance from the crater center, R is crater radius, and T is the ejecta thickness at the rim of the crater. The relation between T and crater radius can be expressed as

$$T = 0.14\,\mathrm{R}^{0.74} \tag{9}$$

As the distance from the crater center is known, the ejecta thickness can be estimated using the above two equations.

By analyzing the trend of the rays in the CE-2 DOM image, the distal ejecta over the CE-4 landing regions are most probably from Finsen, Von Kármán L, and several other craters (*2*). Table S1 shows the estimated thickness for the major ejecta-contributors at the CE-4 landing site using the ejecta thickness model, showing that ejecta thickness at the CE-4 landing site is ~8.1 m, which is comparable with that estimated by Huang *et al.* (*2*).

SUPPLEMENTARY MATERIALS

Supplementary material for this article is available at http://advances.sciencemag.org/cgi/content/full/6/9/eaay6898/DC1

Fig. S1. CE-4 landing site.
Fig. S2. Data processing procedure of LPR high frequency.
Fig. S3. Comparison of high-frequency LPR data between CE-3 and CE-4.
Fig. S4. Velocity estimation using point targets.
Fig. S5. Bulk density versus depth in the first 8 m.
Fig. S6. Joint probability density function of loss tangent as a function of bulk density and oxide content.
Fig. S7. Estimation of the ejecta thickness using DHCs and non-DHCs.
Fig. S8. Geological context and topography at CE-4 landing site.
Table S1. Estimated ejecta thickness at the CE-4 landing site from Finsen, Von Kármán L, and Von Kármán L' craters.
Table S2. The data IDs for the images used in the figures.

REFERENCES AND NOTES

1. H. Hiesinger, J. W. Head, New views of lunar geoscience: An introduction and overview. *Rev. Mineral. Geochem.* **60**, 1–81 (2006).
2. J. Huang, Z.-Y. Xiao, J. Flahaut, M. Martinot, J. W. Head, X. Xiao, M.-G. Xie, L. Xiao, Geological characteristic of Von Kármán Crater, Northwestern South Pole Aitken Basin: Chang'E 4 Landing Site Region. *J. Geophys. Res.* **123**, 1684–1700 (2018).
3. J. M. Reynolds, *An Introduction to Applied and Environmental Geophysics* (John Wiley & Sons, 2011).
4. W. J. Peeples, W. R. Sill, T. W. May, S. H. Ward, R. J. Phillips, R. L. Jordan, E. A. Abbott, T. J. Killpack, Orbital radar evidence for lunar subsurface layering in Maria Serenitatis and Crisium. *J. Geophys. Res.* **83**, 3459–3468 (1978).
5. T. Ono, A. Kumamoto, H. Nakagawa, Y. Yamaguchi, S. Oshigami, A. Yamaji, T. Kobayashi, Y. Kasahara, H. Oya, Lunar radar sounder observations of subsurface layers under the nearside maria of the Moon. *Science* **323**, 909–912 (2009).
6. W. H. Ip, Y. Jun, C.-L. Li, Z.-Y. Ouyang, Preface: The Chang'e-3 lander and rover mission to the Moon. *Res. Astron. Astrophys.* **14**, 1511–1513 (2014).
7. W.-Z. Fa, M.-H. Zhu, T.-T. Liu, J.-B. Plescia, Regolith stratigraphy at the Chang'E-3 landing site as seen by lunar penetrating radar. *Geophys. Res. Lett.* **42**, 10179–10187 (2015).
8. L. Xiao, P.-M. Zhu, G.-Y. Fang, Z.-Y. Xiao, Y.-L. Zou, J.-N. Zhao, N. Zhao, Y.-F. Yuan, L. Qiao, X.-P. Zhang, H. Zhang, J. Wang, J. Huang, Q. Huang, Q. He, B. Zhou, Y.-C. Ji, Q.-Y. Zhang, S.-X. Shen, Y.-X. Li, Y.-Z. Gao, A young multilayered terrane of the northern Mare Imbrium revealed by Chang'E-3 mission. *Science* **347**, 1226–1229 (2015).
9. J. Zhang, W. Yang, S. Hu, Y. Lin, G. Fang, C. Li, W. Peng, S. Zhu, Z. He, B. Zhou, H. Lin, J. Yang, E. Liu, Y. Xu, J. Wang, Z. Yao, Y. Zou, J. Yan, Z. Ouyang, Volcanic history of the Imbrium basin: A close-up view from the lunar rover Yutu. *Proc. Natl. Acad. Sci. U.S.A.* **112**, 5342–5347 (2015).
10. C. Li, S. Xing, S. E. Lauro, Y. Su, S. Dai, J. Feng, B. Cosciotti, F. D. Paolo, E. Mattei, Y. Xiao, C. Ding, E. Pettinelli, Pitfalls in GPR data interpretation: False reflectors detected in Lunar radar cross sections by Chang'e-3. *IEEE Trans. Geosci. Remote Sens.* **56**, 1325–1335 (2018).
11. W. Wu, C. Li, W. Zuo, H. Zhang, J. Liu, W. Wen, Y. Su, X. Ren, J. Yan, D. Yu, G. Dong, C. Wang, Z. Sun, E. Liu, J. Yang, Z. Ouyang, Lunar farside to be explored by Chang'e-4. *Nat. Geosci.* **12**, 222–223 (2019).
12. C. Li, D. Liu, B. Liu, X. Ren, J. Liu, Z. He, W. Zuo, X. Zeng, R. Xu, X. Tan, X. Zhang, W. Chen, R. Shu, W. Wen, Y. Su, H. Zhang, Z. Ouyang, Chang'E-4 initial spectroscopic identification of lunar far-side mantle-derived materials. *Nature* **569**, 378 (2019).
13. D. E. Stuart-Alexander, "Geologic map of the central far side of the Moon" (IMAP 1047, U.S. Geological Survey, 1978).
14. J. H. Pasckert, H. Hiesinger, C. H. van der Bogert, Lunar farside volcanism in and around the South Pole–Aitken basin. *Icarus* **299**, 538–562 (2018).
15. Z. Xiao, Size-frequency distribution of different secondary crater populations: 1. Equilibrium caused by secondary impacts. *J. Geophys. Res.* **121**, 2404–2425 (2016).
16. G.-Y. Fang, B. Zhou, Y.-C. Ji, Q.-Y. Zhang, S.-X. Shen, Y.-X. Li, H.-F. Guan, C.-J. Tang, Y.-Z. Gao, W. Lu, S.-B. Ye, H.-D. Han, J. Zheng, S.-Z. Wang, Lunar penetrating radar onboard the Chang'e-3 mission. *Res. Astron. Astrophys.* **14**, 1607–1622 (2014).
17. Y. Su, G.-Y. Fang, J.-Q. Feng, S.-G. Xing, Y.-C. Ji, B. Zhou, Y.-Z. Gao, H. Li, S. Dai, Y. Xiao, C.-L. Li, Data processing and initial results of Chang'E-3 lunar penetrating radar. *Res. Astron. Astrophys.* **14**, 1623–1632 (2014).
18. M. Angelopoulos, D. Redman, W. H. Pollard, T. W. Haltigin, P. Dietrich, Lunar ground penetrating radar: Minimizing potential data artifacts caused by signal interaction with a rover body. *Adv. Space Res.* **54**, 2059–2072 (2014).
19. H. M. Jol, *Ground Penetrating Radar: Theory and Applications* (Elsevier Science, 2009).
20. S. E. Lauro, E. Mattei, B. Cosciotti, F. Di Paolo, S. A. Arcone, M. Viccaro, E. Pettinelli, Electromagnetic signal penetration in a planetary soil simulant: Estimated attenuation rates using GPR and TDR in volcanic deposits on Mount Etna. *J. Geophys. Res.* **122**, 1392–1404 (2017).
21. W. D. Carrier, G. R. Olhoeft, W. Mendell, Physical properties of the lunar surface, in *Lunar Source-Book: A User's Guide to the Moon*, G. H. Heiken, D. T. Vaniman, B. M. French, Eds. (Cambridge Univ. Press, 1991), chap. 9.
22. G. R. Olhoeft, D. W. Strangway, Dielectric properties of the first 100 meters of the Moon. *Earth Planet. Sci. Lett.* **24**, 394–404 (1975).
23. D. Hickson, A. Boivin, M. G. Daly, R. Ghent, M. C. Nolan, K. Tait, A. Cunje, C. A. Tsai, Near surface bulk density estimates of NEAs from radar observations and permittivity measurements of powdered geologic material. *Icarus* **306**, 16–24 (2018).
24. M. Ohtake, J. Haruyama, T. Matsunaga, Y. Yokota, T. Morota, C. Honda; LISM Team, Performance and scientific objectives of the SELENE (KAGUYA) Multiband Imager. *Earth Planets Space* **60**, 257–264 (2008).
25. P. S. Russell, J. A. Grant, K. K. Williams, L. M. Carter, W. B. Garry, I. J. Daubar, Ground penetrating radar geologic field studies of the ejecta of Barringer Meteorite Crater, Arizona, as a planetary analog. *J. Geophys. Res. Planets* **118**, 1915–1933 (2013).
26. I. Catapano, F. Soldovieri, G. Alli, G. Mollo, L. A. Forte, On the reconstruction capabilities of beamforming and a microwave tomographic approach. *IEEE Geosci. Remote Sens. Lett.* **12**, 2369–2373 (2015).

27. J. L. Whitten, J. W. Head, Lunar cryptomaria: Physical characteristics, distribution, and implications for ancient volcanism. *Icarus* **247**, 150–171 (2015).
28. H. J. Melosh, *Impact Cratering: A Geologic Process* (Oxford Univ. Press, 1989).
29. L. Qiao, Z. Ling, X. Fu, B. Li, Geological characterization of the Chang'e-4 landing area on the lunar farside. *Icarus* **333**, 37–51 (2019).
30. R. A. Yingst, F. C. Chuang, D. C. Berman, S. C. Mest, Geologic mapping of the Planck Quadrangle of the Moon (LQ-29), in *48th Lunar and Planetary Science Conference*, The Woodlands, TX, 20 to 24 March 2017.
31. R. H. Stolt, Migration by Fourier transform. *Geophysics* **43**, 23–48 (1978).
32. S.-G. Xing, Y. Su, J.-Q. Feng, S. Dai, Y. Xiao, C.-Y. Ding, C.-L. Li, The penetrating depth analysis of Lunar Penetrating Radar onboard Chang'e-3 rover. *Res. Astron. Astrophys.* **17**, 046 (2017).
33. N. J. Cassidy, E. S. Calder, A. Pavez, L. Wooller, GPR-derived facies architectures: A new perspective on mapping pyroclastic flow deposits, in *Studies in Volcanology: The Legacy of George Walker* (The Geological Society for IAVCEI, 2009), pp. 181–210.
34. J. Taylor, *Introduction to Error Analysis, the Study of Uncertainties in Physical Measurements* (University Science Books, 1997).
35. J. D. Irving, R. J. Knight, Removal of wavelet dispersion from ground-penetrating radar data. *Geophysics* **68**, 960–970 (2003).
36. Y. Quan, J. M. Harris, Seismic attenuation tomography using frequency shift method. *Geophysics* **62**, 895–905 (1997).
37. A. Tarantola, *Inverse Problem Theory and Methods for Model Parameter Estimation* (Siam, 2005).
38. J. Gazdag, P. Sguazzero, Migration of seismic data. *Proc. IEEE* **72**, 1302–1315 (1984).
39. R. Solimene, I. Catapano, G. Gennarelli, A. Cuccaro, A. Dell'Aversano, F. Soldovieri, SAR imaging algorithms and some unconventional applications: A unified mathematical overview. *IEEE Signal Process. Mag.* **31**, 90–98 (2014).
40. R. Markelein, K. Mayer, R. Hannemann, T. Krylow, K. Balasubramanian, K. J. Langenberg, V. Schmitz, Linear and nonlinear algorithms applied in nondestructive evaluation. *Inv. Probl.* **18**, 1733–1757 (2002).
41. M. Slaney, A. C. Kak, L. E. Larsen, Limitations of imaging with first-order diffraction tomography. *IEEE Trans. Microw. Theory Tech.* **32**, 860–874 (1984).
42. T. R. McGetchin, M. Settle, J. W. Head, Radial thickness variation in impact crater ejecta: Implications for lunar basin deposits. *Earth Planet. Sci. Lett.* **20**, 226–236 (1973).

Acknowledgments: This research was supported by the CE-4 mission of the Chinese Lunar Exploration Program and funded by the National Natural Science Foundation of China (grants nos.11941002 and 41601374). We thank the team members of the Ground Research and Application System, who have contributed to data receiving and release. We thank Dr. Brad Thomson and the other two anonymous reviewers for their very helpful comments. **Author contributions:** C.L., Y.S., E.P., and S.X. designed the research, performed data analysis, and wrote the manuscript. J.L., X.R., D.L., and G.Z. contributed scientific background, geological and geophysical context, and consistency of remote sensing observation. S.D., X.Ze., X.G., W.C., and X.Zh. conducted data preprocessing. C.D., S.E.L., and F.S. analyzed radar images, performed tomographic inversion, and computed electromagnetic parameters. W.Z., W.W., Z.Z., and H.Z. contributed to data management. **Competing interests:** The authors declare that they have no competing interests. **Data and materials availability:** CE-3 radar data (CE3_0005-0007), CE-4 radar data (CE4_0001-0003 and 0005-0010), CE-2 DOM, and CE-4 DOM images are available at Data Publishing and Information Service System of China's Lunar Exploration Program (http://moon.bao.ac.cn). The Kaguya Multiple Imager and Terrain Camera data are available at https://planetarymaps.usgs.gov/mosaic/Lunar_MI_mineral_maps/ and https://darts.isas.jaxa.jp/planet/pdap/selene/. The LROC NAC DTM data are available at http://lroc.sese.asu.edu/data/LRO-L-LROC-5-RDR-V1.0/LROLRC_2001/DATA/SDP/NAC_DTM/. All the data IDs are listed in table S2. All other data needed to evaluate the conclusions in the paper are present in the paper and/or the Supplementary Materials. Additional data related to this paper may be requested from the authors.

Submitted 10 July 2019
Accepted 5 December 2019
Published 26 February 2020
10.1126/sciadv.aay6898

Citation: C. Li, Y. Su, E. Pettinelli, S. Xing, C. Ding, J. Liu, X. Ren, S. E. Lauro, F. Soldovieri, X. Zeng, X. Gao, W. Chen, S. Dai, D. Liu, G. Zhang, W. Zuo, W. Wen, Z. Zhang, X. Zhang, H. Zhang, The Moon's farside shallow subsurface structure unveiled by Chang'E-4 Lunar Penetrating Radar. *Sci. Adv.* **6**, eaay6898 (2020).

Science Advances

The Moon's farside shallow subsurface structure unveiled by Chang'E-4 Lunar Penetrating Radar

Chunlai Li, Yan Su, Elena Pettinelli, Shuguo Xing, Chunyu Ding, Jianjun Liu, Xin Ren, Sebastian E. Lauro, Francesco Soldovieri, Xingguo Zeng, Xingye Gao, Wangli Chen, Shun Dai, Dawei Liu, Guangliang Zhang, Wei Zuo, Weibin Wen, Zhoubin Zhang, Xiaoxia Zhang and Hongbo Zhang

Sci Adv **6** (9), eaay6898.
DOI: 10.1126/sciadv.aay6898